Astronomy & Astrophysics manuscript no. main
April 23, 2025

Tidal phenomena in the Galactic Center: The Curious Case of X7

Wasif Shaqil[1,⋆], Diego Calderón[2,1⋆⋆], Stephan Rosswog[1,3], Jorge Cuadra[4,5], Anna Ciurlo[6], Mark R. Morris[6], Randall D. Campbell[7], and Andrea M. Ghez[6]

[1] University of Hamburg, Hamburger Sternwarte, Gojenbergsweg 112, D-21029 Hamburg, Germany
[2] Max-Planck-Institut für Astrophysik, Karl-Schwarzschild-Straße 1, 85748 Garching, Germany
[3] The Oskar Klein Centre, Department of Astronomy, AlbaNova, Stockholm University, SE-106 91 Stockholm, Sweden
[4] Departamento de Ciencias, Facultad de Artes Liberales, Universidad Adolfo Ibáñez, Av. Padre Hurtado 750, Viña del Mar, Chile
[5] Millennium Nucleus on Transversal Research and Technology to Explore Supermassive Black Holes (TITANS)
[6] Department of Physics and Astronomy, University of California, Los Angeles, CA 90095, USA
[7] W. M. Keck Observatory, Waimea, HI 96743, USA

April 23, 2025

ABSTRACT

Context. Several enigmatic dusty sources have been detected in the central parsec of the Galactic Center. Among them is X7, located at only ∼0.02 pc from the central super-massive black hole, Sagittarius A* (Sgr A*). Recent observations have shown that it is becoming elongated due to the tidal forces of Sgr A*. X7 is expected to be fully disrupted during its pericenter passage around 2035 which might impact the accretion rate of Sgr A*. However, its origin and nature are still unknown.
Aims. We investigated the tidal interaction of X7 with Sgr A* in order to constrain its origin. We tested the hypothesis that X7 was produced by one of the observed stars with constrained dynamical properties in the vicinity of Sgr A*.
Methods. We employed a set of test-particle simulations to reproduce the observed structure and dynamics of X7. The initial conditions of the models were obtained by extrapolating the observationally constrained orbits of X7 and the known stars into the past, making it possible to find the time and source of origin by minimizing the three-dimensional separation and velocity difference between them.
Results. Our results show that ejecta from the star S33/S0-30, launched in ∼1950, can to a large extent, replicate the observed dynamics and structure of X7, provided that it is initially elongated with a velocity gradient across it, and with an initial maximum speed of ∼600 km s^{-1}.
Conclusions. Our results show that a grazing collision between the star S33/S0-30 and a field object such as a stellar mass black hole or a Jupiter-mass object is a viable scenario to explain the origin of X7. Nevertheless, such encounters are rare based on the observed stellar dynamics within the central parsec.

Key words. Galaxy: center – Stars: winds, outflows – Stars: Wolf-Rayet

1. Introduction

The Milky Way Galactic Center (GC) harbors the closest super-massive black hole (SMBH) to Earth: Sagittarius A* (Sgr A*), which has a mass of 4.3×10^6 $M_\odot$ at a distance of 8.3 kpc (GRAVITY Collaboration et al. 2022). This fact makes it a unique laboratory to study the detailed orbital motion of the stellar and gaseous components in the vicinity of a SMBH (see Genzel et al. 2010; Ciurlo & Morris 2025, for a review). Over 30 years of near-infrared (NIR) observations have enabled the monitoring of hundreds of stars with high precision (Schödel et al. 2002; Ghez et al. 2003, 2008; Gillessen et al. 2009, 2017; von Fellenberg et al. 2022), and even to test successfully the predictions of General Relativity (e.g. Do et al. 2019a; Amorim et al. 2019; GRAVITY Collaboration et al. 2020). Currently, there are 195 stars with constrained orbits within the central parsec (von Fellenberg et al. 2022). Many of them correspond to B-type stars (Eisenhauer et al. 2005), and tens of O-type and Wolf-Rayet (WR) stars which have significant mass loss in the form of winds (Paumard et al. 2006; Martins et al. 2007; Habibi et al. 2019). Over the last decade, a lot of attention has been put on the dusty sources known as G objects that coexist with the stars in the vicinity of Sgr A* (e.g. Ciurlo et al. 2023). Despite long observation campaigns and theoretical efforts, their nature remains unknown (see Mapelli & Gualandris 2016; Ciurlo et al. 2020, for a review).

Gillessen et al. (2012) discovered the gaseous and dusty source G2 moving on a highly-eccentric orbit towards Sgr A*. Initially, the source was interpreted as a purely gaseous object with a total mass of merely $3M_\oplus$. Its observed tidal interaction over timescales of the order of years attracted attention due to the potential effect on the quiescent accretion state of Sgr A*. However, there was no clear observed enhancement on the activity of Sgr A* in X-ray (Bouffard et al. 2019) but a bright flare in the near-infrared in 2019 could potentially be attributed to it (Do et al. 2019b; Paugnat et al. 2024). Over the years, many objects of similar characteristics were observed in the central 0.1 pc, increasing the population of G objects up to ten (e.g. Pfuhl et al. 2015; Witzel et al. 2017; Ciurlo et al. 2020; Peißker et al. 2020, 2024b). Many of them show extended emission of the Brγ recombination line at 2.1661 μm and point-source emission in the L′ band at 3.776 μm. None of them show obvious hints for the presence of a stellar object within the extended source. As a result, theoretical efforts have focused on constraining their true nature, especially of G2. But no consensus has been reached on

⋆ Corresponding authors: wasifshaqil@gmail.com
⋆⋆ calderon@mpa-garching.mpg.de

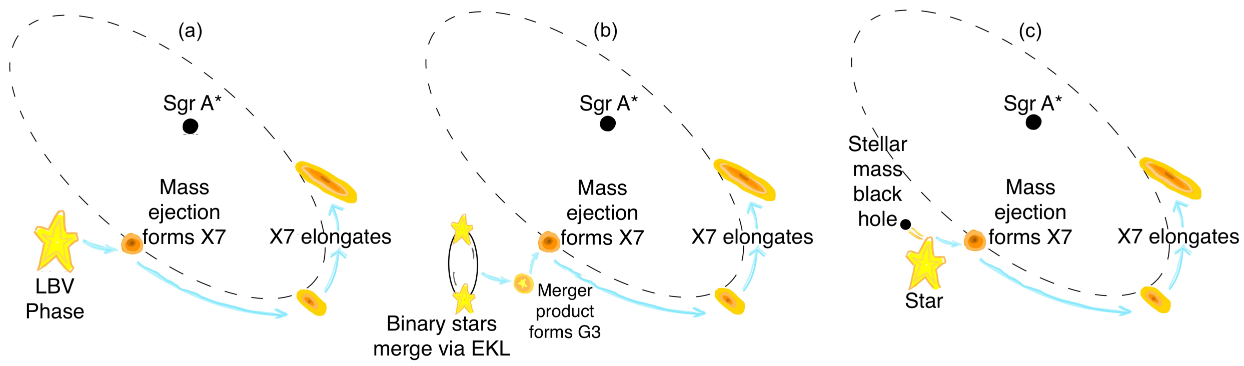

Fig. 1: Schematic representation of the three hypotheses for the origin of X7 studied in this work: (a) X7 formed from a stellar wind of a star during an episode of high mass loss such as a LBV phase. (b) X7 as the ejecta from a stellar merger via the Eccentric Kozai Lidov (EKL) mechanism, where G3 is the merger product due to similar orbital motion. (c) X7 as the ejecta from a collision of a star with a field object such as a stellar mass black hole or a Jupiter-mass object. Bear in mind that the representations are not to scale.

its nature and origin yet. The main debate is focused on whether G2 is a purely gaseous cloud or harbors a compact (stellar) object. In the former, it has been suggested that G2 could be a gas clump formed in stellar wind collisions (Burkert et al. 2012; Calderón et al. 2016), the result of a slow wind from a Luminous Blue Variable (LBV) star (Burkert et al. 2012), or a nova outburst from the partial tidal disruption of a giant star (Meyer & Meyer-Hofmeister 2012), among others. In the latter, G2 has been hypothesized as an evaporating circumstellar disk (Miralda-Escudé 2012; Murray-Clay & Loeb 2012), a proto-planet (Mapelli & Ripamonti 2015), a mass-losing low-mass star (Ballone et al. 2013; De Colle et al. 2014; Valencia-S. et al. 2015; Ballone et al. 2016, 2018), the product of a stellar merger (Witzel et al. 2014; Prodan et al. 2015; Ciurlo et al. 2020), or a young stellar object (YSO; Peißker et al. 2024b). Moreover, Peißker et al. (2024a) also argue for binaries within the G object population.

In this region at a separation of $\sim$0.5″($\sim$0.02 pc) from Sgr A*, the source X7 has been observed to be interacting tidally with the central black hole. Although X7 has certain similarities with the G objects, e.g. it is an extended source made out of gas and dust, it is much larger, reaching $\sim$3300 au in 2021 whereas G-objects are of the order of $\sim$100 au. It was reported for the first time by Clénet et al. (2004) and since then it has been routinely monitored by several groups (Mužić et al. 2007; Peißker et al. 2020, 2021; Ciurlo et al. 2023). Initially, it was thought to be a bow shock but recent observations suggest a morphological deviation from that picture (Ciurlo et al. 2023). Recently, Peißker et al. (2021) proposed that X7 is a circumstellar envelope of the star S50/S0-73 as they were close in earlier observations. However, Ciurlo et al. (2023) argued against that hypothesis by revealing that there is a significant three-dimensional spatial and dynamical separation between them. Additionally, they calculated that the pericenter passage of X7 is estimated to take place around 2035. If X7 is a purely gaseous and dusty source, we will be able to witness the tidal disruption of this object by Sgr A* and consequently enhanced accretion activity of Sgr A*. An alternative scenario has been proposed recently by Peißker et al. (2024b), which suggests both X7 and a similar dusty feature called X3 correspond to YSOs. Nevertheless, the nature of X7 is still unknown and observational and theoretical efforts are ongoing to unravel its mystery.

In this work, we present a study to constrain the origin of X7. We work under the assumption that the source is purely gaseous and dusty, and therefore its age is less than its orbital period of 200 years. We present a set of test-particle simulations and analytical estimates to study how likely it is that X7 was related to any of the stars in the central parsec of the GC. Our results show that the current observations of X7 are consistent with the source being the ejecta resulting from a grazing collision between the S-star S33/S0-30 (an early B-type star) and a field object such as a stellar-mass black hole or a Jupiter-mass object. It has been suggested that X7 could be connected to the G object G3 (Ciurlo et al. 2023), because of the remarkable alignment of their orbits. However, we find that they are most likely not connected since, provided the age of X7 to be less than 200 yrs, they show significantly different orbital phases even considering the large associated uncertainties. This article is organized as follows: in Section 2, we present the properties of X7 as well as the three hypotheses for its formation studied in this work. Section 3 contains the details of the calculations, methods and the numerical setup for testing the hypotheses. In Section 4, we present the results from our analysis and simulations. Section 5 discusses the implication of our results for understanding the origin of X7. Finally, we summarize and conclude this study in Section 6. Throughout this paper, we used $M_{\rm BH} = 4.3 \times 10^6$ M$_\odot$ and $R_0 = 8.3$ kpc, where $M_{\rm BH}$ and R_0 are the mass of Sgr A* and the distance to it from Earth (GRAVITY Collaboration et al. 2022).

2. Hypotheses for the origin of X7

X7 has been monitored continuously since 2002 with telescopes at the W. M. Keck Observatory (Ciurlo et al. 2023) as part of the Galactic Center Orbits Initiative (GCOI; PI: Andrea Ghez). The data traced the dust thermal emission – through images in L′-band (3.776 μm) obtained with the imager NIRC2 - and the gas emission through the Br-γ hydrogen recombination line observed with the integral field spectrograph OSIRIS (Larkin et al. 2006). These observations have shown that the size of X7 has nearly doubled from $L \sim 2000$ au in 2003 to $L \sim 3300$ au in 2021. Additionally, it was possible to fit a Keplerian orbit to its forward tip, revealing a semi-major axis of 4800 ± 1100 au and an eccentricity of 0.34 ± 0.05 (Ciurlo et al. 2023). Under the assumption that it is a purely gas and dust feature, a total mass of $\sim$50 M$_\oplus$ was derived using the observed Br-γ flux. Then, it is straightforward to estimate that the ratio between the derived and Roche densities (the critical density to remain intact against

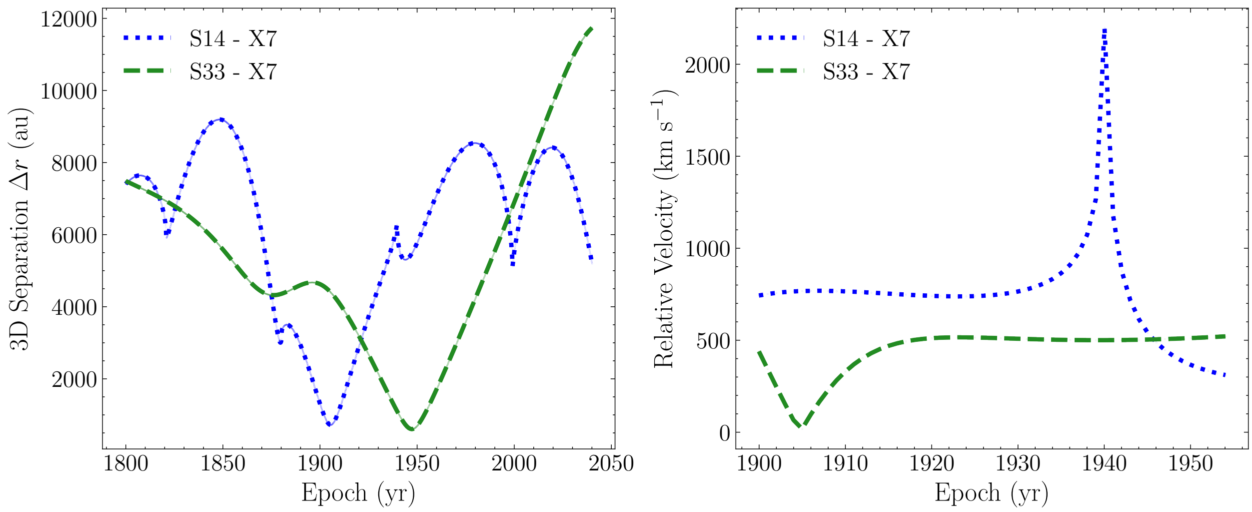

Fig. 2: Three-dimensional separation and relative velocity between stars and X7 as a function of time are shown in the left- and right-hand side panels, respectively. The two stars closest to X7; S14/S0-16 and S33/S0-30 are shown. The case S14/S0-16-X7 is displayed as a dotted blue line while S33/S0-30-X7 is represented as a dashed green line. The calculations are shown in the time period 1800-2050 and 1900-1950 for the left and right panels respectively.

tidal forces of the SMBH) of X7 is very small ($\sim 10^{-5}$). This shows that its self-gravity is negligible provided that no compact source is associated to it. Based on this, its age is constrained to be less than its orbital period (~200 yr), as otherwise the tidal forces would have already destroyed it.

Under the assumption that X7 is only made out of gas and dust, we propose and study three hypotheses to explain its origin.

- First, X7 could be the result of a mass outflow from a massive star going through a high mass-loss episode such as a Luminous Blue Variable (LBV) phase. This scenario is plausible since the central parsec hosts hundreds of O- and B-type stars (e.g. Paumard et al. 2006; Martins et al. 2007; Habibi et al. 2019).
- The second hypothesis conceives X7 as ejecta from a binary merger process. This case is supported by the fact that the sources G3 and X7 could be considered dynamically linked as they move on very similar orbits and share common observational properties (see Ciurlo et al. 2020, 2023). In this scenario, G3 would be the merger product and X7 the mass ejecta from the Eccentric Kozai-Lidov (EKL; Kozai 1962; Lidov 1962; Naoz 2016) induced merger process.
- Third, X7 could be ejecta from a grazing collision of a star with a field object such as a stellar-mass black hole or a Jupiter-mass object (Ciurlo et al. 2023). Here, X7 would be the stripped material unbound from the star during the collision. This is plausible as the stars in the GC are expected to undergo multiple stellar collisions due to the high stellar density (Genzel et al. 1996; Dale et al. 2009). Moreover, the central parsec should contain a large population of stellar-mass black holes due to dynamical mass segregation (Morris 1993; Freitag et al. 2006).

Schematic representations of the hypotheses are shown in Figure 1.

3. Analysis

Regardless of the hypothesis considered, all of them have in common that X7 would be related to a stellar source in the region. Hence, as a first step we proceed to investigate which stars could be linked to X7 based on their dynamics. It is to be noted that, when we mention the orbit of X7, we refer to the orbit of its tip (Ciurlo et al. 2023). Once we find the best star candidate to be related to X7, we simulate the dynamical evolution of a cloud of test particles launched from the position and time of the closest encounter. In this section, we describe in detail these calculations.

3.1. Correlation with stars in the Galactic Center

First, we analyzed whether X7 is related to one of the stars in the vicinity of Sgr A*. Thus, we searched for stars that were close simultaneously in space and time from X7 by tracing their orbits back in time into the past. To do so, we assumed that the orbits have not changed significantly in the last 200 years. This is a reasonable assumption since the dominant gravitational field is due to Sgr A*. Currently, there are 36 stars with fully constrained orbital parameters and 159 stars with constrained orbits but incomplete orbital solutions (z-coordinate missing) (von Fellenberg et al. 2022). Following the `MINECC` method in Cuadra et al. (2008), we looked for the minimum eccentricity possible for each of the 159 stars and considered the corresponding value of z in order to model their orbits. By doing so, we have a total of 195 stars with orbits for our analysis.

We traced back their orbits for the period 1800−2024 and selected the stars having the closest three-dimensional distance to X7 at some point during this time. To select the best candidates, we chose that the three-dimensional distance of closest approach must be <1000 au, and their relative velocities at that time had to be <1000 km s^{-1}. Following this procedure, we found two stars: S14/S0-16 and S33/S0-30, both of which have fully determined orbital solutions (von Fellenberg et al. 2022). Figure 2 shows the three-dimensional separation (left panel) and relative velocity (right panel) of these two stars with respect to X7 as a function of time during the period 1800 – 2050. In the case of S14/S0-16 (dotted blue line), the closest approach to X7 was in ~1905 at a separation and a relative velocity of Δr ~727 au and Δv ~760 km s^{-1}, respectively. In the case of S33/S0-30 (dashed green line), the shortest distance was $\Delta r \sim 610$ au and the relative velocity $\Delta v \sim 505$ km s^{-1} in the year ~1947. It is to be noted

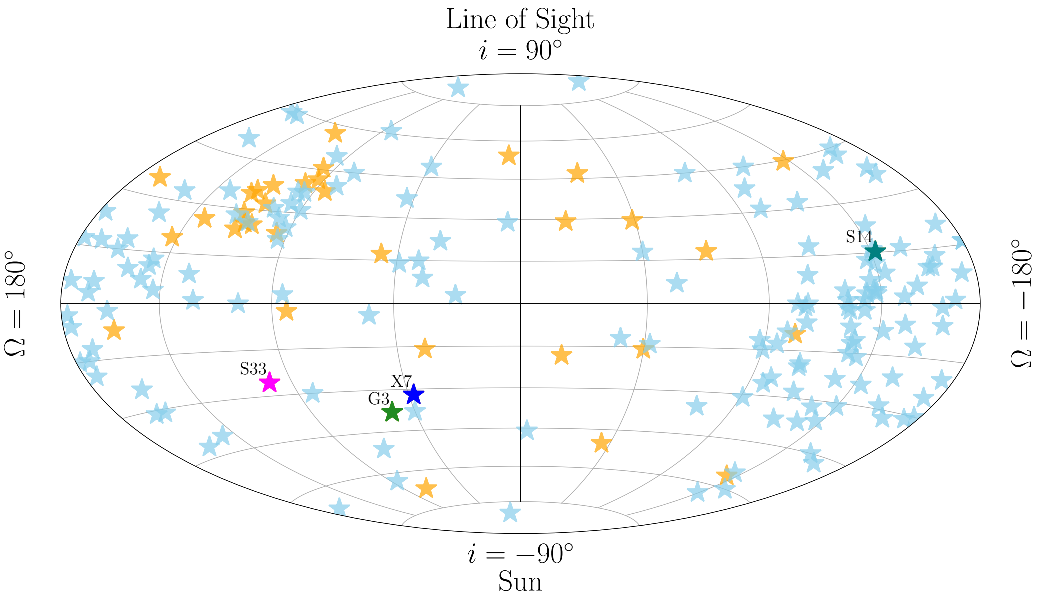

Fig. 3: Hammer projection of the orientation of the angular momentum vectors of the stars with full (orange star symbols) and incomplete (sky-blue star symbols) orbital solutions. The vertical dimension represents the inclination of the orbit i and the horizontal dimension represents the longitude of the ascending node Ω. A face-on star in a clockwise orbit will be at the top of the hammer projection and an edge-on star will be at the equator. The bottom half shows the counter-clockwise orbits. S14/S0-16, S33/S0-30, X7, and G3 are shown as teal, magenta, blue, and green star symbols, respectively.

that other assumptions to constrain the missing z coordinate of the stars with incomplete orbits were explored. Specifically, we sampled all possible values of z compatible with the observational constraints and found no other candidate that satisfied the criteria.

As a next step, we inspected the angular momentum direction of the candidate stars and X7. Figure 3 is a Hammer projection that shows the orbital angular momentum direction for all stars in our sample as well as the sources X7 and G3 (Ciurlo et al. 2020, 2023). The stars with completely determined orbits are shown as orange star symbols while the rest of the 159 are displayed as sky-blue star symbols. S14/S0-16, S33/S0-30, X7, and G3 are highlighted as teal, magenta, blue, and green star symbols, respectively. Notice that S14/S0-16 has a very different angular momentum orientation compared to both X7 and G3, whereas S33/S0-30 is much closer to X7 and G3 in the Hammer projection. In principle, this points to S33/S0-30 being a more promising candidate for being related to X7. Despite some stars having similar angular momentum orientation to X7, it is important to bear in mind that they have a large minimum three-dimensional separation to X7 (> 6000 au), so they are unlikely to be related. Gillessen et al. (2009, 2017) have characterized the star S33/S0-30 as an early-type star that is part of the S-star cluster. Unfortunately, we are not aware of additional information on this star.

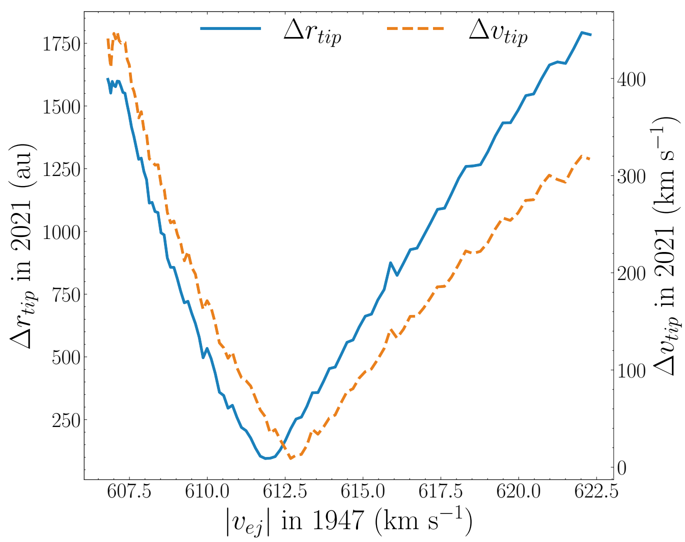

Fig. 4: Three-dimensional separation $\Delta r_{\rm tip}$ and relative velocity $\Delta v_{\rm tip}$ between the tip of the simulated cloud and X7 in 2021 as a function of the magnitude of initial velocity $|v_{\rm ej}|$ of the simulated cloud. The solid blue and dashed orange lines represent $\Delta r_{\rm tip}$ and $\Delta v_{\rm tip}$, respectively. Notice that both quantities have a minimum at $|v_{\rm ej}| \sim 612$ km s^{-1}.

3.2. Test-particle simulations

We model the evolution of a cloud represented with test particles launched from the position and time of the closest encounter between S33/S0-30 and X7. First, we describe the numerical setup and technique. Then, we calculate the initial conditions for the simulations such as initial velocity, direction, radius, and shape of the cloud.

3.2.1. Numerical Setup

The simulations considered the dynamical evolution of a cloud represented with test particles under the influence of the gravitational field of Sgr A*. The equations of motion were integrated numerically using a leapfrog algorithm with a timestep that is a

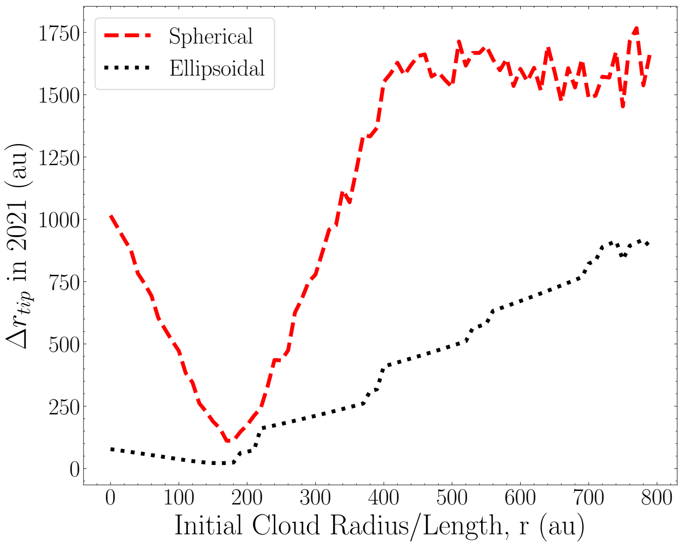

Fig. 5: Three-dimensional separation of the tip of the simulated cloud and X7 in 2021 ($\Delta r_{\rm tip}$) as a function of the initial size of the simulated cloud. The dotted black and dashed red lines represent the initial length of the ellipsoidal and initial radius of the spherical clouds, respectively

Table 1: Summary of the results of our simulations using different initial configurations. All starting from the initial position of S33/S0-30 in 1947, and running till the present time. The uncertainties are 1σ deviations from the mean based on 10000 simulation runs.

Sim ID	$N_{\rm runs}$	$N_{\rm particles}$	$\Delta r_{\rm tip}$ (au)	$\Delta v_{\rm tip}$ (km s^{-1})
$\rm sp_{uniform}$	10000	10-10000	116±8	42±6
$\rm sp_{Gaussian}$	10000	10-10000	250±21	102±6
Ellipsoidal	10000	10-10000	50±21	22±6

small fraction of the circular orbital time scale at separation R,

$$\Delta t = C\sqrt{\frac{R^3}{GM_{\rm BH}}}$$

where R is the radial distance of the particle to the location of Sgr A*, $M_{\rm BH}$ is the mass of the SMBH, G is the gravitational constant, and C is the prefactor which is set to $C = 0.01$ for accuracy. We have applied an adaptive time-stepping scheme where the minimum timestep Δt out of all the particles at each iteration is considered. The initial position of the cloud was set to the position of S33/S0-30 in 1947. Then, it is only necessary to specify the size of the cloud and its initial velocity.

3.2.2. Initial velocity

To find the initial velocity of the cloud, we calculated the velocity required for ejecta from the position $\boldsymbol{r}$ of S33/S0-30 in 1947 to achieve the same observed specific angular momentum $\boldsymbol{l}$ of the tip of X7. To do so, we solved the following equation to find $\boldsymbol{v}_{\rm X7}(t = 1947)$,

$$\boldsymbol{l}_{\rm X7} = \boldsymbol{r}_{\rm S33/S0\text{-}30}(t = 1947) \times \boldsymbol{v}_{\rm X7}(t = 1947) \quad (1)$$

This corresponds to a system of linear equations obtained that is not independent, so a unique solution is not possible. However, for each value of v_z there are unique values of v_x and v_y. The components v_x and v_y can be obtained from the below equations,

$$v_x = -\left[442 + \left(\frac{v_z}{1.8\ \rm km\ s^{-1}}\right)\right]\ \rm km\ s^{-1}, \quad (2)$$

$$v_y = \left[699 + \left(\frac{v_x}{1.6\ \rm km\ s^{-1}}\right)\right]\ \rm km\ s^{-1}. \quad (3)$$

Then, we sampled a wide range of values for v_z from -10000 km s^{-1} and 10000 km s^{-1} with a step size of 1 km s^{-1}. In this way, the velocity magnitude will be of the same order as the typical velocities of the stars in the GC. To select the optimal initial velocity and its direction, we selected the velocities that minimize the three-dimensional separation and relative 3D velocity between the tip of the simulated cloud and the observed tip of X7 in 2021, which are represented as $\Delta r_{\rm tip}$ and $\Delta v_{\rm tip}$, respectively. Figure 4 shows $\Delta r_{\rm tip}$ and $\Delta v_{\rm tip}$ as a function of the magnitude of the initial velocity $|\boldsymbol{v}_{\rm ej}|$ in 1947. It is important to remark that only a zoomed version of the region around the minima is shown. Here it is possible to observe that an initial velocity of ~ 612 km s^{-1} minimizes both the $\Delta r_{\rm tip}$ and $\Delta v_{\rm tip}$.

For a range of v_z, between $(-40 < v_z < -30)$ km s^{-1}, the optimal range of components of initial velocity, having an initial velocity magnitude of ~ 610 km s^{-1}, is between

$$(-426 < v_x < 420)\ \rm km\ s^{-1} \quad \& \quad (433 < v_y < 436)\ \rm km\ s^{-1} \quad (4)$$

By optimal, we mean that the separation of the tip of the simulated cloud and the observed tip of X7 ($\Delta r_{\rm tip}$) is less than 175 au (~21 mas), which falls within the margin of error in the 2021 observations from Ciurlo et al. (2023).

3.2.3. Cloud structure and size

We investigated the cases of a spherical cloud uniformly sampled, a spherical cloud sampled following a three-dimensional Gaussian distribution, and an ellipsoidal cloud uniformly sampled. Here we focus on the case of the ellipsoidal cloud as it gave the most relevant results. We refer the reader to the Appendix A to see the results of the spherical cloud cases. In the ellipsoidal cloud case, we set up a cloud with N particles that are uniformly distributed along a length of $L = 200$ au, with the semi-major axis $a = L/2$. There is negligible dependency on the other two semi-major axes (b and c), as long as they are less than a. Moreover, for each particle, we set the polar angle $0° < \theta < 90°$ and the azimuthal angle $0° < \phi < 180°$. These two angles have, in practice, no effect on our overall results. The initial position of the tip of the cloud $\boldsymbol{r}_{\rm tip}^{\rm initial} = (x_0,\ y_0,\ z_0)$ is assigned from the position of S33/S0-30 in 1947. The position of the rest of the $N-1$ particles were assigned by adding the position of each particle from the center of the ellipsoid (x, y, z) to the initial position,

$$\texttt{initial\_position[i]} = (x_0 + x[i], y_0 + y[i], z_0 + z[i])$$

To assign the initial velocity of each particle, we have used a coefficient of linear increase k in au yr^{-1} dx^{-1} such that there is a velocity spread from tip to tail. Moreover, we used an initial position angle of $\theta_{\rm ini} = 75°$ for the ridge of the ellipsoid obtained after testing angles between $0° < \theta < 90°$. In order to find the initial cloud size we tested initial lengths from 1 au to 800 au and analyzed the three dimensional separation of the tip of the simulated cloud and X7 in 2021. Figure 5 shows $\Delta r_{\rm tip}$ as a function of the initial ellipsoid length. The ellipsoidal and spherical cases are shown as dotted black and dashed red lines, respectively. In both the cases, it is possible to observe that an initial length/radius of ~200 au minimizes $\Delta r_{\rm tip}$ in 2021.

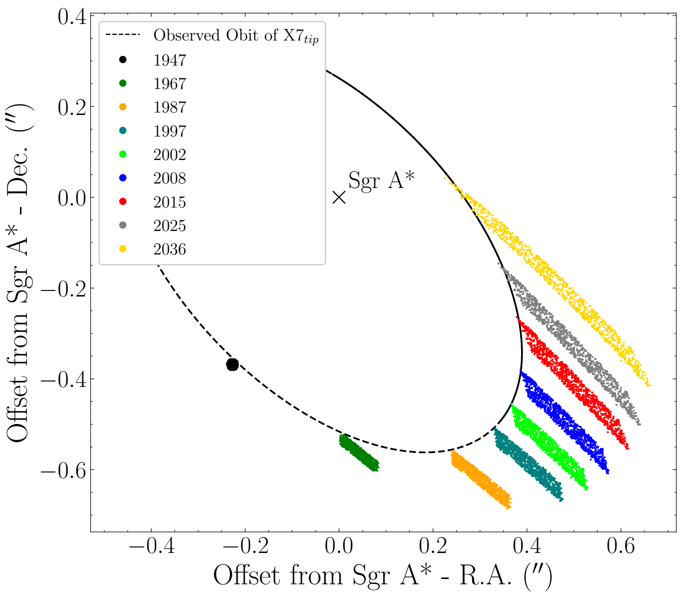

Fig. 6: Test-particle simulation of an uniformly sampled ellipsoidal cloud launched from the position of S33/S0-30 in 1947. Each color represents different times through its dynamical evolution. The sky-projected observed orbit of the tip of X7 is represented as the black dashed line. As a reference, Sgr A* is marked with a cross at the origin.

In Table 1, we have summarized the different initial configurations for our simulations, their corresponding three-dimensional separation, and relative velocity in 2021. We also tested different number of particles to represent the cloud $N_{\mathrm{particles}}$ between 10 and 10000. We found that this does not affect the results in a significant way.

4. Results

In this section, we proceed to present the results of the simulations with the optimal initial conditions obtained previously. The result of one of the realizations is shown in Figure 6. This shows the sky-projected evolution of the initially ellipsoidal cloud where different colors represent the structure at different simulation times. We find that the cloud becomes more elongated through time and maintains a roughly constant position angle of ~45° from 2002 until its pericenter passage around ~2035.

4.1. X7 modeled evolution with S33/S0-30 as progenitor

Figure 7 shows the sky-projected orbits of X7 and the tip of the simulated cloud for each set of optimal velocities as dashed solid and gray dotted lines, respectively. As a reference, Sgr A* is represented as a black cross at the origin and the initial position of the tip of the cloud is displayed as a red square. The observed tip of X7 and of the simulated clouds in 2021 are shown as a purple cross and green triangles, respectively. The light blue shaded region shows the 68% confidence interval of the best-fit of the observed orbit of X7. The sky-projected orbits have a strong correspondence (by construction) with the observed orbit, the three-dimensional spatial difference of ~50 au (see Table 1), is well within the uncertainty as reported by Ciurlo et al. (2023). Moreover, the best realization implies a position of the tip of the simulated cloud at 0.348″ and -0.151″ in 2021 in offsets from Sgr A* in right ascension and declination, respectively, both of

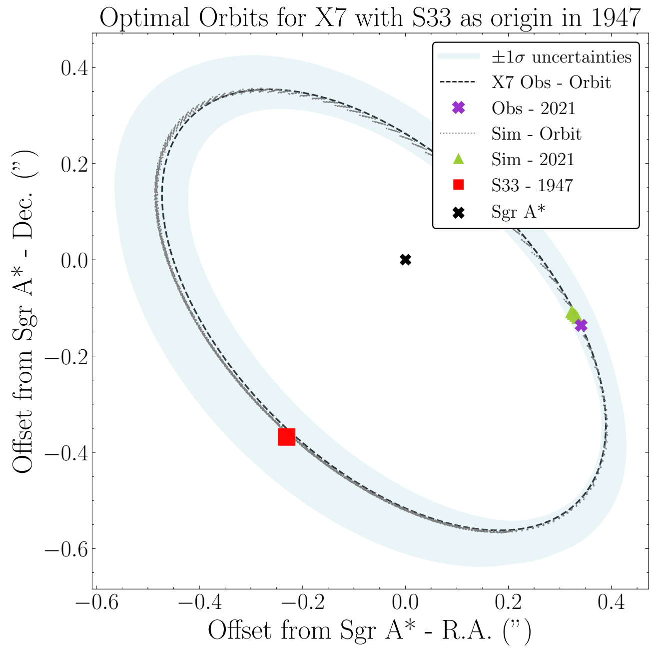

Fig. 7: Comparison of the sky-projected orbits and position in 2021 of X7 and the tip of the simulated clouds. The black dashed line shows the best-fit orbit of the tip of X7, the light-blue shaded region shows the uncertainties with a 68% confidence interval, and the purple cross marks its position in 2021 (Ciurlo et al. 2023). The dotted gray lines show the orbit of the simulated clouds for each of the optimal velocities. The red squares and light green triangles show the position of the tip of the simulated clouds in 1947 and 2021, respectively.

which are within the error bars of the 2021 measurements by Ciurlo et al. (2023).

Figure 8 shows the spatial and dynamical evolution of the simulated cloud during the period of the observations from 2002 to 2021. The left-hand side panel shows the sky-projected morphology evolution of the cloud where the colors represent the particles from tip to tail. The observed orientation of X7 at different epochs is displayed as thick gray lines (the length is not to scale). As a reference, the position of Sgr A* is represented with a black cross in the upper left corner, the orbit of X7 is shown as a dashed black line, and the simulated orbit is displayed as a dashed gray line. This configuration is obtained only if the ellipsoidal cloud is initialized with a initial length ~200 au, and position angle $\theta_{\mathrm{ini}} \sim 75°$. Notice that the simulated cloud maintains a relatively constant orientation throughout the observational period from 2002 to 2021. Although the agreement with the observed orientation of X7 is not perfect, it is off by $< 10°$. Additionally, the length of the simulated cloud is consistent with the observed length of X7 in 2021 which is ~3300 au. The right-hand side panel shows the line-of-sight velocity of the simulated cloud as a function of time. The colors represent the corresponding particles in the left panel. This analysis shows that there is a crossover of the radial velocity from tip to tail around 2018. In this case, the radial velocity of the tip decelerates by $\sim 200\ \mathrm{km\ s^{-1}}$ (see evolution of the black band), whereas the relative velocity of the tail remains relatively constant till ~2021 (see evolution of yellow markers). It is important to remark that the observations of X7 shows exactly the same behavior although at a slightly different time (Ciurlo et al. 2023).

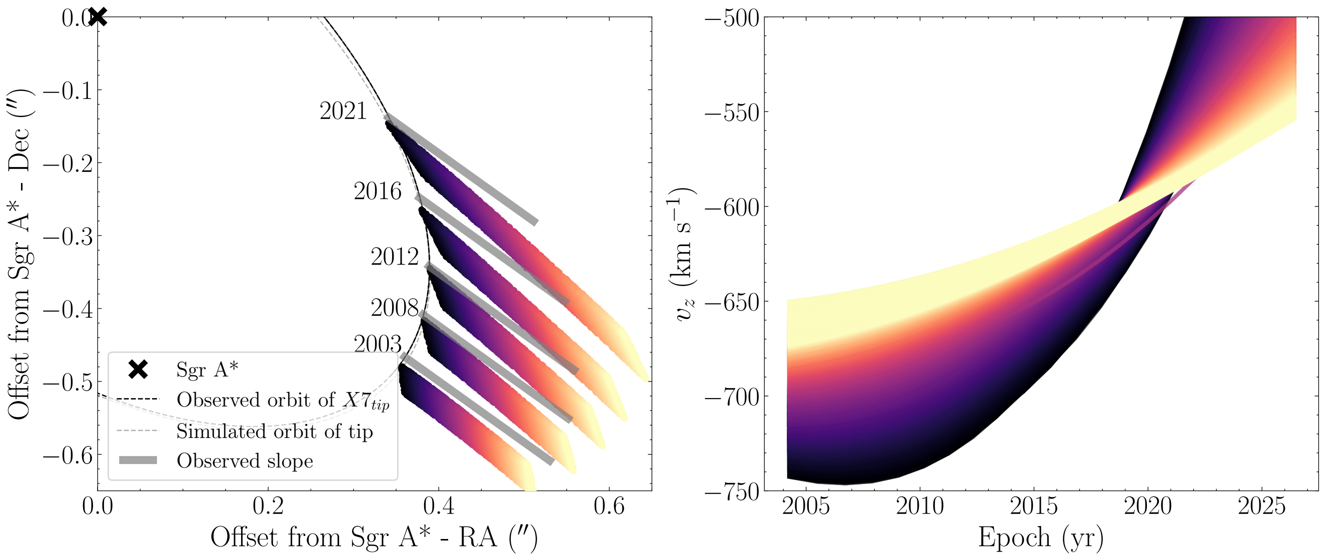

Fig. 8: Evolution of the inclination and line-of-sight velocity for the best-fitting simulated cloud during the period of the observations. Left panel: sky projection of the simulated cloud at t = 2003, 2008, 2012, 2016, and 2021 yr. The particles are colored from tip to tail from black to yellow. The gray shaded lines show the observed slope of the ridge of X7 at the same epochs (length not to scale). Right panel: line-of-sight velocity of the particles as a function of time. The colors represent the corresponding particles shown in the left panel. This figure is analogous to Figure 10 of Ciurlo et al. (2023).

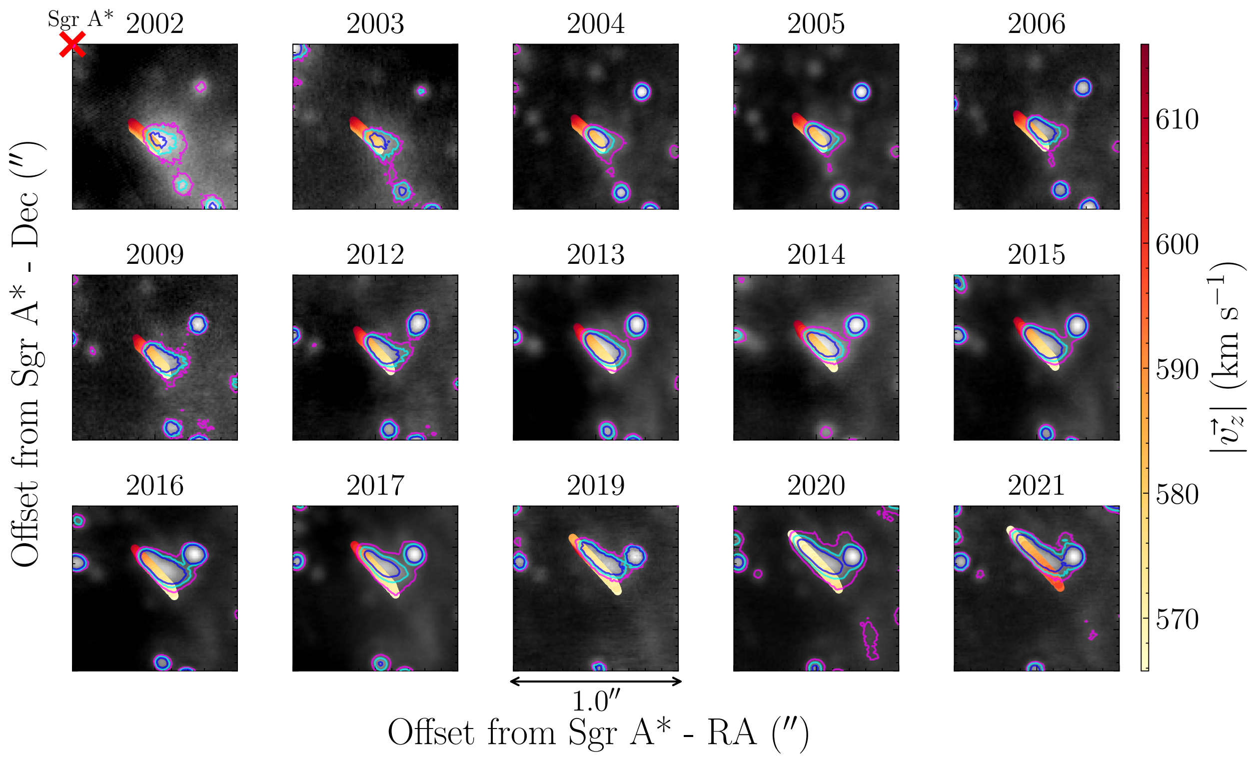

Fig. 9: Comparison of the morphological evolution of X7 and the simulated cloud. The panels show 1$''$× 1$''$ L$'$-band images highlighting the emission from X7 with contours in the period 2002-2021. The simulated cloud is overlaid with colored markers that encode the line-of-sight velocity. The position of Sgr A* is on the top left corner of each panel. North and East directions are up and left, respectively.

4.2. Comparison with observational data

Figure 9 shows a comparison of the morphological evolution of X7 observed in the L$'$-band and the simulated cloud during the period 2002-2021. Each panel shows an image of the sky of an area of 1$''$ × 1$''$, where Sgr A* is located in the top left corner. North and East directions are up and left, respectively. The emission of X7 is shown with contour lines and the simulated cloud is overlaid with colored markers representing the line-of-sight velocity. In 2002, X7 had a much rounder shape than the simulated cloud which is already elongated. At later times, the

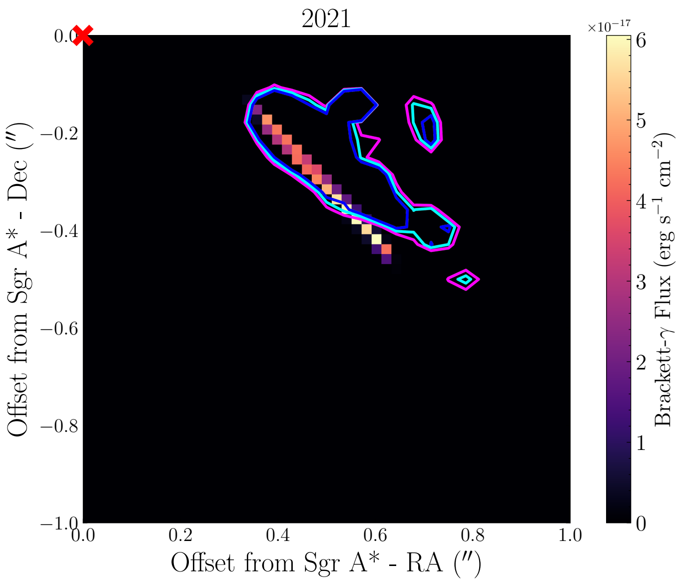

Fig. 10: Comparison of the morphology of X7 and the simulated cloud through the observed (contours) and simulated (colormap) Br-γ images in 2021. The contour levels represent 0.25 (blue), 0.275 (cyan), 0.30 (magenta) of the Br-γ emission maximum. The sky area shown is 1″× 1″ with Sgr A* located on the uppermost left-hand side corner of the plot.

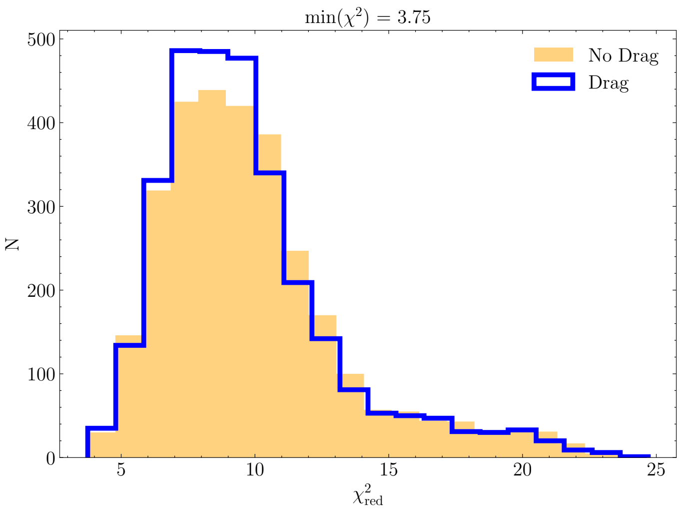

Fig. 11: Histogram of the $\chi^2_{\rm red}$ distribution of the 3000 realizations of the simulated cloud with initial conditions obtained from sampling the posterior distribution of the orbital fit of X7. The solid blue line and orange area represent the results of the fiducial case and the one considering the drag force of the ambient medium, respectively. The minimum value is $\chi^2_{\rm red}$ = 3.75 in both cases.

observations of X7 display a more elongated morphology that visually tends to align with the simulated cloud. This is clearer after 2015 when most of the observed shape of X7 is contained within the sky-projected simulated cloud. The agreement is best in the last epoch although this is not surprising since the initial velocity was selected so that tip of the cloud reproduces the position of X7 at this time.

In order to make a quantitative comparison, we calculated the reduced chi-square parameter $\chi^2_{\rm red}$ for the tip of the simulated cloud and X7 considering the three-dimensional position and velocity across every single observation epoch. Additionally, we took into account the 1σ uncertainties in the orbital fit of X7. Thus, we conducted 3000 realizations of this procedure sampling the initial conditions from the posterior distribution of the orbital fit of X7. Figure 11 shows the $\chi^2_{\rm red}$ distribution of this procedure. This analysis also includes the impact of a hypothetical drag force due to the interaction of the cloud with the ambient medium (see Section 4.3.3). The distribution shows that the median value of $\chi^2_{\rm red}$ ∼ 8 and a minimum value of $\chi^2_{\rm red}$ = 3.75. Overall, the model can reproduce the observed orbit of X7 to a large extent. This result is not significantly affected by the drag force of the medium.

In order to make a more appropriate comparison of the model with observational data we synthesized the Br-γ emission from the simulated cloud. Following Case B recombination theory, the Br-γ emissivity can be estimated following Schartmann et al. (2015) as

$$j_{Br\gamma} = 3.44\times10^{-27}\left(\frac{T}{10^4\ \mathrm{K}}\right)^{-1.09}\ \mathrm{erg\ s^{-1}\ cm^{-3}} \tag{5}$$

The total emissivity is calculated by multiplying by $n_{\rm e}n_{\rm p}$, where $n_{\rm e}$ and $n_{\rm p}$ are the electron and proton number density of the cloud. We can obtain the corresponding flux observed from Earth by integrating over the volume element, then scaling by the inverse square law as

$$F_\lambda = \frac{\int j_{\rm Br\gamma}\, n_{\rm e} n_{\rm p}\, dV}{4\pi R_0^2} \tag{6}$$

where V is the volume of the cloud, and R_0 = 8300 pc is the distance to the GC. Figure 10 shows a comparison of the sky-projected observed and simulated Br-γ flux in 2021 as a colormap and contours, respectively. Notice that most of the simulated emission is spatially contained within the observational contours of 0.3 of the maximum emission. The simulated cloud is noticeably thinner which could be a result of not taking into account the instrument point-spread function. For completeness, a complete comparison of the evolution of the Br-γ flux during the period 2006-2021 is shown in Figure C.1. Quantitatively, the total flux obtained from our simulated cloud is $\sim 1.28\times10^{-15}$ erg s^{-1} cm^{-2}, whereas the total observed flux from X7 is 3.55×10^{-15} erg s^{-1} cm^{-2} in 2021 (Ciurlo et al. 2023). In summary, the model produces a cloud of similar morphology and emission of the same order of magnitude of the observations.

4.3. Secondary effects

Up to now, our models have considered solely the effect of the gravitational field of Sgr A*. In this section, we study the effects of other mechanisms that could play a role in the dynamical evolution of X7. First, we estimate the impact of stellar winds from the Wolf-Rayet (WR) stars. Within the central parsec, there are ∼30 WR stars with strong mass loss of $\sim10^{-5}$ M$_\odot$ yr^{-1} launched at 500-2500 km s^{-1} (Martins et al. 2007; Cuadra et al. 2008). Secondly, we investigate the effect of an outflow launched from the central region. The accretion flow of Sgr A* has been described successfully as a radiatively inefficient accretion flow (RIAF) due to both its inability to radiate its energy and the small fraction of the gas that ends up being accreted (e.g. Genzel et al. 2010). In this scenario, the flow gets overheated and part of it can be launched as an energetic mass outflow (Blandford & Begelman 1999; Begelman 2012). Assuming such an outflow indeed

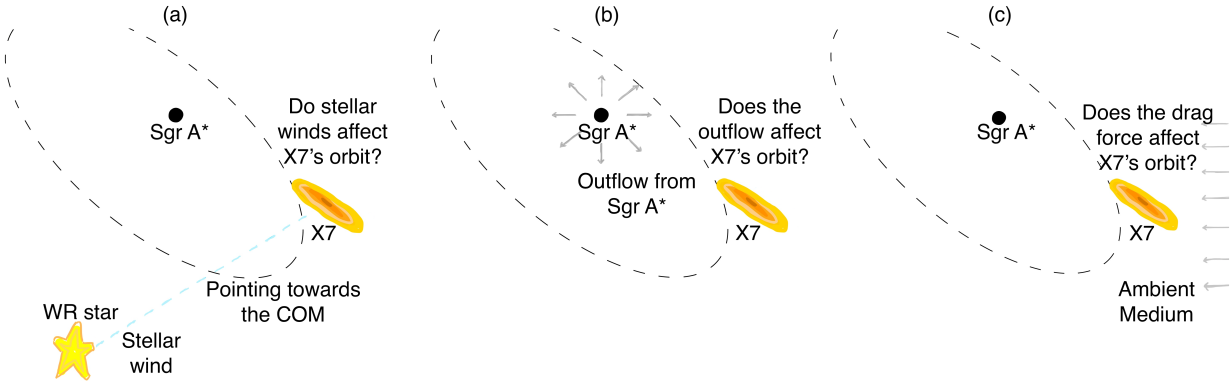

Fig. 12: Schematic representation of the secondary effects which could affect the dynamical evolution of X7. (a) Ram pressure due to stellar winds pointing towards the center of mass of X7. (b) Ram pressure due to a spherical outflow from Sgr A*. (c) Drag force of the medium (ISM) in the vicinity of X7. Not to scale.

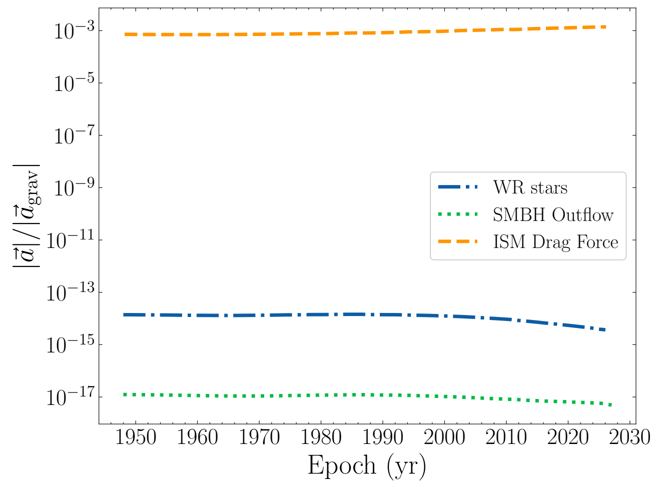

Fig. 13: Ratio of magnitude of the acceleration on the simulated cloud due to secondary effects and gravity as a function of time. The effects of the stellar winds of the five closest WR stars, an outflow from Sgr A*, and the drag of the medium are shown as dashed orange, dotted green, and dotted-dashed blue lines, respectively.

took place in the GC we can also estimate its impact on the evolution of X7. At last, we consider the effect of a drag force due to the interaction between the object and the ambient medium. This can alter the orbits of the test particles that represent X7 in our model. Schematic representation of these effects are shown in Figure 12.

4.3.1. Stellar winds from Wolf-Rayet stars

To date, ~30% of the stars in the central parsec of the GC have complete orbital solutions (von Fellenberg et al. 2022). Thus, for the rest we used the solutions obtained by minimizing their orbital eccentricity (see Section 3.1). Then, we found the closest WR stars to X7 since the year 1947 until 2021. We considered only the five WR stars with closest approach to X7 in that period, namely E40, E48, E80, E81, and E83 (in UCLA nomenclature: S3-5, IRS13 E4, S9-9, S9-283 and S10-5, respectively; Paumard et al. 2006). These stars have winds with mass-loss rates of the order of few 10^{-5} $M_\odot$ $\rm yr^{-1}$ and velocities in the range 800-1000 km $\rm s^{-1}$ (Martins et al. 2007; Cuadra et al. 2008). The ram pressure exerted by the stellar winds on X7 is given by $P_{\rm w} = \rho_{\rm w} v^2_{\rm w,X7}$, where $v_{\rm w,X7}$ is the net velocity of the wind acting on X7 taking into account the relative velocity of X7 and the WR star. The density of the stellar wind, assumed to be spherically symmetric and stationary, is denoted by ρ_w and is given by,

$$\rho_{\rm w} = \frac{\dot{M}}{4\pi V_{\rm w} R^2} \tag{7}$$

where $\dot{M}$ is the stellar wind mass-loss rate, $V_{\rm w}$ is the terminal velocity of the stellar wind, and R is the distance from the star. By adding an additional term as a source of acceleration due to the ram pressure in our simulation, we can estimate whether stellar winds from WR stars can affect the evolution of the cloud. Then, the new equation of motion is given by

$$\frac{d^2\boldsymbol{r}}{dt^2} = -\frac{GM_{\rm BH}}{r^2}\hat{\boldsymbol{r}} - \frac{\sigma_{\rm c}}{m_{\rm c}}\rho_{\rm w}\left|\frac{dr}{dt}\right|^2\hat{\boldsymbol{v}} \tag{8}$$

where σ_c and m_c are the cross section in the direction of the net velocity vector $v_{\rm w,X7}$ and mass of X7, respectively. Then, we simulated a simple model where the net stellar wind is pointed towards the center of mass (COM) of the cloud. The results show that the motion of the simulated cloud does not change significantly. Figure 13 shows the ratio of the stellar wind and the gravitational accelerations as a function of the simulation time as a dotted-dashed blue line. Here it is possible to observe that this value remains roughly constant around 10^{-14}. This shows that their effect is negligible during this time period.

4.3.2. Outflow from the SMBH

We performed a similar analysis as in Section 4.3.1 but considering a spherically symmetric outflow launched from the location of Sgr A*. The exact mass loss rate and velocity of the outflow were set to $\dot{M}_{\rm BH} = 10^{-4}$ $M_\odot$ $\rm yr^{-1}$ and $v_{\rm out} = 10^9$ cm $\rm s^{-1}$, respectively and motivated by numerical simulations of this process (e.g. Cuadra et al. 2015). Our simulation shows that the evolution of the orbit of the simulated cloud is not affected significantly by the outflow. The relative magnitude of this acceleration compared to the gravitational acceleration as a function of time is shown in Figure 13 as a dotted green line. The value is of the order of 10^{-17} which is even smaller than the effect of the stellar winds and, therefore, is also negligible. Moreover, even a much stronger outflow will have a negligible effect on the orbit of X7. It is relevant to mention that this result is in agreement with the analysis in Ciurlo et al. (2023), as they argued that the morphology of X7 cannot be explained by an outflow from Sgr A*.

4.3.3. The effect of a static drag force

To account for the relative motion of the ambient medium we also investigated the effect of a static drag force acting against the motion of the cloud. This has been taken into account previously for the G2 object (Madigan et al. 2017; Calderón et al. 2018), and later observed by (Gillessen et al. 2019). In principle, this would cause deviations from the Keplerian orbits of the test particles of the simulated cloud. In this case, the equation of motion becomes,

$$\frac{d^2\boldsymbol{r}}{dt^2} = -\frac{GM_{\rm BH}}{r^2}\hat{\boldsymbol{r}} - \frac{\sigma_{\rm c}}{m_{\rm c}}\rho_{\rm ISM}(r)\left|\frac{d\boldsymbol{r}}{dt}\right|^2\hat{\boldsymbol{v}} \tag{9}$$

where G is the gravitational constant, $M_{\rm BH}$ is the mass of Sgr A*, $m_{\rm c}$ and σ_c are the mass and cross section of the cloud, and $\hat{\boldsymbol{r}}$ and $\hat{\boldsymbol{v}}$ are the unit vectors in the radial and velocity directions, respectively. The density of the ambient medium $\rho_{\rm ISM}$ is considered using the model by Yuan et al. (2003) which reproduces the Chandra X-ray observations and is consistent with the latest model by Roberts et al. (2017). This density profile is given by,

$$\rho_{\rm ISM}(r) = 10^{-22}\left(\frac{1.7\times10^{17}}{r}\right)^{\alpha}\ \text{g cm}^{-3} \tag{10}$$

where α is the power-law index. Moreover, the mass of the cloud is constrained to $\sim$50 $M_\oplus$ (Ciurlo et al. 2023). Then, assuming that the masses of the particles are identical, the mass of each particle is determined.

In this case, the drag force affects the orbit of the test particles. The dashed orange line in Figure 13 shows the ratio of the drag force and gravitational accelerations as a function of time. Here it can be seen that the value is $\sim10^{-3}$ which is much larger than in the previous cases. This effect results in changes in the position of the tip of the simulated cloud that increases the three-dimensional separation of the simulated tip and X7 in 2021. Specifically, the fiducial model results in a separation of $\sim$50 au while the calculations with the drag force shows it to be $\sim$130 au. However, there is no significant change in the length of the cloud. Although $\Delta r_{\rm tip}$ increases, the result is still within the margin of the errors. Thus, this effect does not impact significantly the overall results. It is to be noted that a non-static drag force could have slightly different effects (Madigan et al. 2017).

5. Discussion

We have shown that ejecta from S33/S0-30 provided with an ejection velocity of $\sim$610 km s^{-1} in 1947 can reproduce the orbit of X7 such that the tip of the simulated cloud and the observed tip of X7 in 2021 have a separation, $\Delta r_{\rm tip}$, of around 50 au. We have also shown that an initially elongated cloud with an initial velocity gradient can reproduce the observed orientation of X7 (see Figure 8). In this section, we interpret these results based on our proposed hypotheses for the origin of X7.

5.1. A star in an extensive mass-losing phase

We started with the hypothesis that X7 formed when a star in the past 200 years went through a phase of excessive mass loss such as a Luminous-Blue-Variable phase. The abundance of O-type and WR stars in the galactic center support this idea, since it is possible for a O-type star to go through a LBV phase before becoming a WR star (e.g. Crowther 2007). The WR stars in the GC have a mass loss rate of a few 10^{-5} $M_\odot$ yr^{-1} (Martins et al. 2007). With this rate, it would take approximately 15 years to lose an amount of mass comparable to the mass of X7. However, the best candidate to be the origin of X7, S33/S0-30, is a B-type star whose mass-loss rates are not as high ($\lesssim10^{-8}$ $M_\odot$ yr^{-1}; Martins et al. 2008). Even if the mass-loss rates were to go an order or two higher, the timescale needed is very long to generate a single coherent structure comparable to X7. Moreover, such a mass-loss will occur in a spherically-symmetric manner, whereas our model favors an ellipsoidal ejecta. Based on this, it is very unlikely for X7 to have originated in this way.

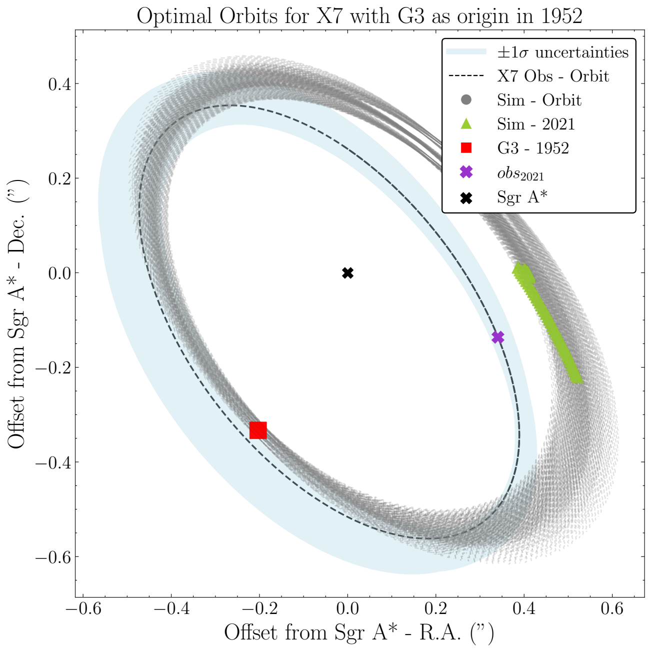

Fig. 14: Comparison of the sky-projected orbits and position in 2021 of X7 and the tip of the simulated clouds from G3 in 1952. The black dashed line shows the best-fit orbit of the tip of X7, the light-blue shaded region shows the uncertainties with a 68% confidence interval, and the purple cross marks its position in 2021 (Ciurlo et al. 2023). The dotted gray lines show the orbit of the simulated clouds for each of the optimal velocities. The red squares and light green triangles show the position of the tip of the simulated clouds in 1952 and 2021, respectively.

5.2. Ejecta from a stellar merger: are X7 and G3 dynamically linked?

Since X7 and G3 have similar orbits and emission characteristics they have been hypothesized to have been formed in an EKL induced merger scenario where G3 is the merger product and X7 is the ejected mass (Ciurlo et al. 2023). Notice that even the orientations of the angular momentum of X7 and G3 are strikingly similar (see Figure 3). To test this hypothesis, we did a similar analysis as the one done for S33/S0-30 and X7. We extrapolated the orbit of G3 and X7 backwards in time in order to find their closest separation over the last 200 yr period. As a result, we found that this occurred on two occasions: in $\sim$1880 and $\sim$1952. However, we noticed that G3 is always orbiting ahead of X7 on the sky. Their three-dimensional separation in the closest encounters is larger than 1200 au. Even taking the cases of the closest encounters as the origin of the simulated cloud, we ended up obtaining significant differences between the expected position of the tip of the simulated cloud and X7 in 2021. In the cases of 1880 yr and 1952 yr, we found that the separations are ~40000 au and ~1200 au between their tips, respectively. When we consider the uncertainties in the orbit of X7, the three-dimensional separation remains of the same order of magnitude in both cases. Moreover, the sky-projected position for the best cases in 1952 are offset beyond the uncertainties as shown in Figure 14.

These results show that ejecta from G3 in 1880 or 1952 cannot be placed on an orbit like the one observed for X7. Thus, it is difficult to reconcile the idea of X7 being ejecta from G3 over the last 200 yr. We note that this conclusion relays on the current orbital estimates of X7 and G3 which have relatively large uncertainties due to short orbital phase coverage ($\lesssim$10%; Ciurlo et al. 2023).

5.3. Grazing collision of a star with a field object

The case of the grazing collision of a star and a field object such as a stellar mass black hole or even a Jupiter-mass object has been discussed in detail by Ciurlo et al. (2023). Such collisions of red giants and compact remnants have also been shown to explain the depletion of red giants within the inner 10″ of the Galactic center (Davies et al. 2011). In principle, a grazing collision of a red giant with any such field objects can account for the mass of X7 by stripping enough material from the star's atmosphere (Ciurlo et al. 2023). This is an interesting prospect since our simulations show that an initially elongated ejecta from S33/S0-30 with an ejection velocity of 610 km s^{-1} can indeed be placed on an orbit similar to X7's and can reproduce its observed tail orientation (see Figure 8). However, if that were to be the case, the star would be left in an agitated state and would only settle down in the Kelvin-Helmholtz timescale (Ciurlo et al. 2023). There is no account of such effects for S33/S0-30. Moreover, it is hard to explain the existence of other gas and dust sources similar to X7 in the Galactic center, as the collision rate between the red giants and field objects could be as low as once in every 10^5 years (Rose et al. 2020, 2022, 2023). Albeit being unlikely, our results show a good agreement with this scenario.

5.4. An infalling gas filament

An additional hypothesis not studied yet is considering X7 as a gaseous clump or stream resulting from the many stellar wind collisions that take place in the vicinity of Sgr A*. Although single stellar wind collisions have been shown to produce only light clumps ($\lesssim$0.01 $M_\oplus$; Calderón et al. 2020a), in principle the simultaneous interaction of more stellar winds could result in larger and/or more massive structures. Hydrodynamic simulations of the WR stellar winds feeding Sgr A* have been performed by many authors (Cuadra et al. 2005, 2006, 2008, 2015; Russell et al. 2017; Ressler et al. 2018; Calderón et al. 2020b; Ressler et al. 2020; Solanki et al. 2023; Balakrishnan et al. 2024; Calderón et al. 2025). Here, we analyzed the hydrodynamic models developed by Calderón et al. (2025) in order to search for cold and gaseous structures that might share properties with X7. We selected an output of the simulation that corresponds to the last observation of X7, i.e. t = 2021. Then, we analyzed the region within 10″ (~0.4 pc) from Sgr A*. We imposed constraints on gas temperature of <10^5 K, inclination $-90° < i < 0°$, and longitude of ascending node $-180° < \Omega < 0°$ in order to find cold structures oriented similarly to that of X7. The results of this analysis are shown as a Hammer projection in Figure 15. Here it is possible to observe that there seem to be cells with similar angular momentum direction to X7's. However, we checked whether such cells form a coherent spatial structure and found that these are not spatially connected. Thus, it is unlikely that X7 has originated from Wolf-Rayet stellar wind interactions.

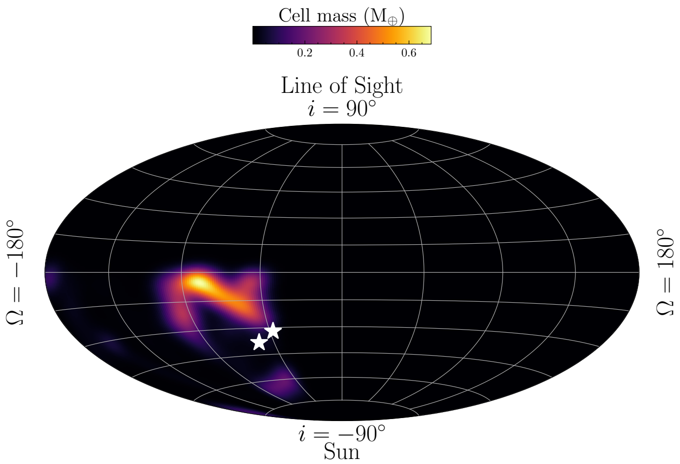

Fig. 15: Density map of the gas structures in the RAMSES simulation for the stellar winds from the Wolf-Rayet stars feeding the black hole (Calderón et al. 2025). The gas cells having $T < 10^5$ K, inclination $-90° < i < 0°$, and longitude of ascending node $-180° < \Omega < 0°$ are considered to find coherent structures having similar orientation of the orbital angular momentum to that of X7 and G3. Colorbar refers to cell mass. None of the gas cells form any coherent clumps which could evolve into X7.

6. Conclusion

We have studied the dynamical evolution of the source X7 in order to constrain its origin. Under the assumption that this object is purely a gas and dust feature, we tested three scenarios for its formation: from the wind of a star going through a high mass-loss episode, as the ejecta of a binary merger, or as the ejecta from the grazing collision of a star with a stellar-mass black hole or Jupiter-mass object. In order to test these hypotheses, we analyzed 195 stars with observationally constrained orbits within the central parsec of the GC. We searched for suitable progenitors with closest approach to X7 of <1000 au, relative velocities of <1000 km s^{-1} over the last 200 years, and similar angular momentum orientation. According to these criteria, we found only one suitable candidate: the star S33/S0-30 (Gillessen et al. 2009, 2017; von Fellenberg et al. 2022). This star and X7 had their closest approach in the year 1947 with a minimum separation and relative velocity of ~600 au and ~500 km s^{-1}, respectively. We have modelled the evolution of hypothetical ejecta with a set of test particles launched from the position of S33/S0-30 in 1947 with an initial velocity that minimizes the difference between the three-dimensional distance and relative velocity between the simulated cloud and X7. This analysis shows that:

1. It is unlikely for X7 to have formed from a stellar wind. No star with sufficiently high mass loss has been close enough to its position over the last 200 years.

2. Despite their similar orbits X7 and G3 do not seem to be related, as extrapolating their positions to the past does not result in close encounters, and neither can ejecta from G3 form the orbit of X7. It is relevant to bear in mind that this conclusion relies on the age of X7 being less than its orbital period of ~200 years.
3. Initially elongated ejecta of length $L = 200$ au from the star S33/S0-30 with an initial velocity of 610 km s^{-1} and an initial velocity gradient from tip to tail, can be placed on a similar orbit to X7's, and reproduce the current position of its tip. Additionally, the length of such ejecta is ~3350 au in 2021 which is consistent with the observational data.
4. Secondary effects such as stellar wind ram pressure, and hypothetical feedback event from the SMBH are not significant to affect the evolution of X7. A static ISM drag can indeed change the orbit of X7 but it does not affect its dynamics significantly over the simulated timescale of ~80 yr.

From these results, we speculate that a grazing collision between S33/S0-30 and a field object such as a stellar-mass black hole or a Jupiter-mass object could have produced the ejecta that corresponds to X7. It will be interesting to observe the star S33/S0-30 for any extended dusty envelope which could further strengthen our results. As X7 approaches the pericenter passage, it will elongate more and begin fragmenting, which has already been observed. Our simulations are fairly accurate before the pericenter passage. To reveal more about the tidal interaction and post-pericenter evolution, numerical hydrodynamic simulations are required. Future observations will reveal more interesting properties with better constraints.

Acknowledgements. WS and JC acknowledge the kind hospitality of the Max Planck Institute for Astrophysics where part of this work was developed. The research of WS, DC, and SR has been funded by the Deutsche Forschungsgemeinschaft (DFG, German Research Foundation) under Germany's Excellence Strategy - EXC 2121 - "Quantum Universe" - 390833306. Since 01.10.2024, DC has been funded by the Alexander von Humboldt Foundation. SR has also been supported by the Swedish Research Council (VR) under grant number 2020-05044, by the research environment grant "Gravitational Radiation and Electromagnetic Astrophysical Transients" (GREAT) funded by the Swedish Research Council (VR) under Dnr 2016-06012, by the Knut and Alice Wallenberg Foundation under grant Dnr. KAW 2019.0112, and by the European Research Council (ERC) Advanced Grant INSPIRATION under the European Union's Horizon 2020 research and innovation programme (Grant agreement No. 101053985). JC acknowledges financial support from ANID – FONDECYT Regular 1211429 and 1251444, and Millennium Science Initiative Program NCN2023_002. The analysis and visualizations in this work made use of Python libraries, Numpy (Harris et al. 2020) and Matplotlib (Hunter 2007). RAMSES hydrodynamical simulation data analysis was carried out using the Python library YT (Turk et al. 2011).

Data Availability

Available on reasonable request to the corresponding author.

References

Amorim, A., Bauböck, M., Berger, J. P., et al. 2019, Phys. Rev. Lett., 122, 101102
Balakrishnan, M., Russell, C. M. P., Corrales, L., et al. 2024, ApJ, 974, 99
Ballone, A., Schartmann, M., Burkert, A., et al. 2013, ApJ, 776, 13
Ballone, A., Schartmann, M., Burkert, A., et al. 2018, MNRAS, 479, 5288
Ballone, A., Schartmann, M., Burkert, A., et al. 2016, ApJ, 819, L28
Begelman, M. C. 2012, MNRAS, 420, 2912
Blandford, R. D. & Begelman, M. C. 1999, MNRAS, 303, L1
Bouffard, É., Haggard, D., Nowak, M. A., et al. 2019, ApJ, 884, 148
Burkert, A., Schartmann, M., Alig, C., et al. 2012, ApJ, 750, 58
Calderón, D., Ballone, A., Cuadra, J., et al. 2016, MNRAS, 455, 4388
Calderón, D., Cuadra, J., Russell, C. M. P., et al. 2025, A&A, 693, A180
Calderón, D., Cuadra, J., Schartmann, M., et al. 2018, MNRAS, 478, 3494
Calderón, D., Cuadra, J., Schartmann, M., et al. 2020a, MNRAS, 493, 447
Calderón, D., Cuadra, J., Schartmann, M., Burkert, A., & Russell, C. M. P. 2020b, ApJ, 888, L2
Ciurlo, A., Campbell, R. D., Morris, M. R., et al. 2023, ApJ, 944, 136
Ciurlo, A., Campbell, R. D., Morris, M. R., et al. 2020, Nature, 577, 337
Ciurlo, A. & Morris, M. R. 2025, arXiv e-prints, arXiv:2503.20081
Clénet, Y., Rouan, D., Gendron, E., et al. 2004, A&A, 417, L15
Crowther, P. A. 2007, ARA&A, 45, 177
Cuadra, J., Nayakshin, S., & Martins, F. 2008, MNRAS, 383, 458
Cuadra, J., Nayakshin, S., Springel, V., & Di Matteo, T. 2005, MNRAS, 360, L55
Cuadra, J., Nayakshin, S., Springel, V., & Di Matteo, T. 2006, MNRAS, 366, 358
Cuadra, J., Nayakshin, S., & Wang, Q. D. 2015, MNRAS, 450, 277
Dale, J. E., Davies, M. B., Church, R. P., & Freitag, M. 2009, MNRAS, 393, 1016
Davies, M. B., Church, R. P., Malmberg, D., et al. 2011, in Astronomical Society of the Pacific Conference Series, Vol. 439, The Galactic Center: a Window to the Nuclear Environment of Disk Galaxies, ed. M. R. Morris, Q. D. Wang, & F. Yuan, 212
De Colle, F., Raga, A. C., Contreras-Torres, F. F., & Toledo-Roy, J. C. 2014, ApJ, 789, L33
Do, T., Hees, A., Ghez, A., et al. 2019a, Science, 365, 664
Do, T., Witzel, G., Gautam, A. K., et al. 2019b, ApJ, 882, L27
Eisenhauer, F., Genzel, R., Alexander, T., et al. 2005, ApJ, 628, 246
Freitag, M., Amaro-Seoane, P., & Kalogera, V. 2006, ApJ, 649, 91
Genzel, R., Eisenhauer, F., & Gillessen, S. 2010, Reviews of Modern Physics, 82, 3121
Genzel, R., Thatte, N., Krabbe, A., Kroker, H., & Tacconi-Garman, L. E. 1996, ApJ, 472, 153
Ghez, A. M., Duchêne, G., Matthews, K., et al. 2003, ApJ, 586, L127
Ghez, A. M., Salim, S., Weinberg, N. N., et al. 2008, ApJ, 689, 1044
Gillessen, S., Eisenhauer, F., Trippe, S., et al. 2009, ApJ, 692, 1075
Gillessen, S., Genzel, R., Fritz, T. K., et al. 2012, Nature, 481, 51
Gillessen, S., Plewa, P. M., Eisenhauer, F., et al. 2017, ApJ, 837, 30
Gillessen, S., Plewa, P. M., Widmann, F., et al. 2019, ApJ, 871, 126
GRAVITY Collaboration, Abuter, R., Aimar, N., et al. 2022, A&A, 657, L12
GRAVITY Collaboration, Abuter, R., Amorim, A., et al. 2020, A&A, 636, L5
Habibi, M., Gillessen, S., Pfuhl, O., et al. 2019, ApJ, 872, L15
Harris, C. R., Millman, K. J., van der Walt, S. J., et al. 2020, Nature, 585, 357
Hunter, J. D. 2007, Computing in Science and Engineering, 9, 90
Kozai, Y. 1962, AJ, 67, 591
Larkin, J., Barczys, M., Krabbe, A., et al. 2006, in Society of Photo-Optical Instrumentation Engineers (SPIE) Conference Series, Vol. 6269, Ground-based and Airborne Instrumentation for Astronomy, ed. I. S. McLean & M. Iye, 62691A
Lidov, M. L. 1962, Planet. Space Sci., 9, 719
Madigan, A.-M., McCourt, M., & O'Leary, R. M. 2017, MNRAS, 465, 2310
Mapelli, M. & Gualandris, A. 2016, in Lecture Notes in Physics, Berlin Springer Verlag, ed. F. Haardt, V. Gorini, U. Moschella, A. Treves, & M. Colpi, Vol. 905, 205
Mapelli, M. & Ripamonti, E. 2015, ApJ, 806, 197
Martins, F., Genzel, R., Hillier, D. J., et al. 2007, A&A, 468, 233
Martins, F., Gillessen, S., Eisenhauer, F., et al. 2008, ApJ, 672, L119
Meyer, F. & Meyer-Hofmeister, E. 2012, A&A, 546, L2
Miralda-Escudé, J. 2012, ApJ, 756, 86
Morris, M. 1993, ApJ, 408, 496
Murray-Clay, R. A. & Loeb, A. 2012, Nature Communications, 3, 1049
Mužić, K., Eckart, A., Schödel, R., Meyer, L., & Zensus, A. 2007, A&A, 469, 993
Naoz, S. 2016, ARA&A, 54, 441
Paugnat, H., Do, T., Gautam, A. K., et al. 2024, ApJ, 977, 228
Paumard, T., Genzel, R., Martins, F., et al. 2006, ApJ, 643, 1011
Peißker, F., Ali, B., Zajaček, M., et al. 2021, ApJ, 909, 62
Peißker, F., Hosseini, S. E., Zajaček, M., et al. 2020, A&A, 634, A35
Peißker, F., Zajaček, M., Labadie, L., et al. 2024a, Nature Communications, 15, 10608
Peißker, F., Zajaček, M., Melamed, M., et al. 2024b, A&A, 686, A235
Pfuhl, O., Gillessen, S., Eisenhauer, F., et al. 2015, ApJ, 798, 111
Prodan, S., Antonini, F., & Perets, H. B. 2015, ApJ, 799, 118
Ressler, S. M., Quataert, E., & Stone, J. M. 2018, MNRAS, 478, 3544
Ressler, S. M., Quataert, E., & Stone, J. M. 2020, MNRAS, 492, 3272
Roberts, S. R., Jiang, Y.-F., Wang, Q. D., & Ostriker, J. P. 2017, MNRAS, 466, 1477
Rose, S. C., Naoz, S., Gautam, A. K., et al. 2020, ApJ, 904, 113
Rose, S. C., Naoz, S., Sari, R., & Linial, I. 2022, ApJ, 929, L22
Rose, S. C., Naoz, S., Sari, R., & Linial, I. 2023, ApJ, 955, 30
Russell, C. M. P., Wang, Q. D., & Cuadra, J. 2017, MNRAS, 464, 4958
Schartmann, M., Ballone, A., Burkert, A., et al. 2015, ApJ, 811, 155
Schödel, R., Ott, T., Genzel, R., et al. 2002, Nature, 419, 694
Solanki, S., Ressler, S. M., Murchikova, L., Stone, J. M., & Morris, M. R. 2023, ApJ, 953, 22
Turk, M. J., Smith, B. D., Oishi, J. S., et al. 2011, ApJS, 192, 9
Valencia-S., M., Eckart, A., Zajaček, M., et al. 2015, ApJ, 800, 125
von Fellenberg, S. D., Gillessen, S., Stadler, J., et al. 2022, ApJ, 932, L6
Witzel, G., Ghez, A. M., Morris, M. R., et al. 2014, ApJ, 796, L8
Witzel, G., Sitarski, B. N., Ghez, A. M., et al. 2017, ApJ, 847, 80
Yuan, F., Quataert, E., & Narayan, R. 2003, ApJ, 598, 301

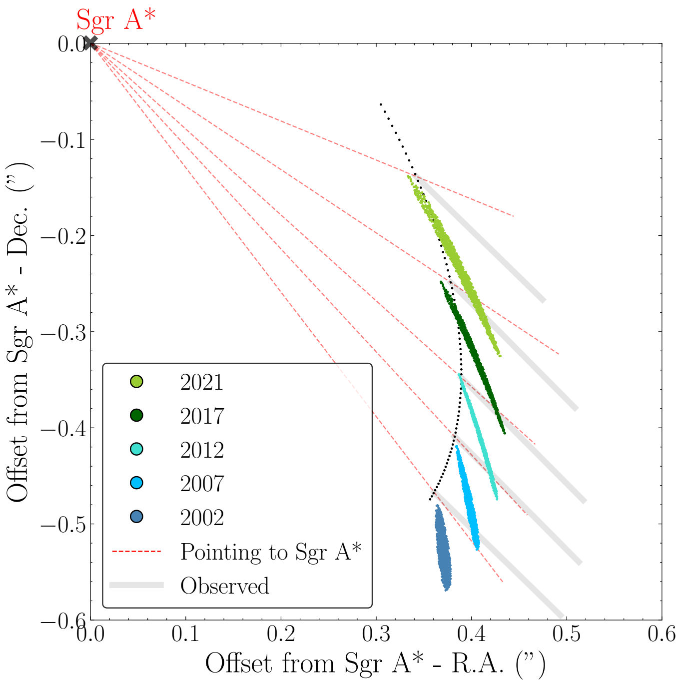

Fig. A.1: Comparison of the orientation of the initially spherical simulated cloud and X7. The sky-projected morphology of the simulated cloud is shown at $t = 2002, 2007, 2012, 2017$, and 2021 yr as dark blue, light blue, cyan, dark green, and light green dots, respectively. The gray shaded lines show the observed orientation of X7 (Ciurlo et al. 2023). The red dashed line represents the lines connecting Sgr A* and the location of the tip of X7 at a given epoch. The location of Sgr A* is on the uppermost left-hand side corner.

Appendix A: Spherical initial configuration

In the main text, we presented the result of simulations that considered an initially ellipsoidal cloud as that showed the best agreement with the observations. For completeness, here we included the results considering a uniform initially spherical cloud. This simulation resulted in a three-dimensional separation between the simulated cloud and the observed tips of X7 of $\Delta r_{\rm tip} \sim 116$ au in 2021. The length of the simulated cloud was ~2000 au in 2021 whereas the observations show a length of ~3300 au (Ciurlo et al. 2023). However, the main discrepancy comes from the orientation of the tail of the simulated cloud and X7. Figure A.1 shows the sky-projected morphology of the simulated cloud at $t = 2002, 2007, 2012, 2017$, and 2021 yr as dark blue, light blue, cyan, dark green, and light green dots, respectively. The gray shaded lines indicate the orientation of the observed structure of X7 (Ciurlo et al. 2023). The dashed red lines are lines connecting Sgr A* and the observed positions of the tip of X7 at the reported times. The location of Sgr A* is on the uppermost left-hand side corner. The disagreement between the orientation of the simulated and observed structures is clear. The discrepancy is around $\sim 20° - 40°$ during the epoch 2002-2021 yr.

Moreover, we tested the initially spherical cloud case with a three-dimensional Gaussian distribution structure as well (see Table 1). This case resulted in $\Delta r_{\rm tip}$ ~250 au, and relative velocities of ~100 km s^{-1} in 2021. Additionally, the mismatch of the simulated cloud and X7 orientation was even more prominent.

Appendix B: A different orbit for X7

Peißker et al. (2024b) derived a different orbit for X7 when compared to the one by Ciurlo et al. (2023). A comparison between these orbits can be seen on the left-hand side panel of Figure B.1. The solid red and black lines represent the orbits inferred by Ciurlo et al. (2023) and Peißker et al. (2024b), respectively. It is clear that there is a large discrepancy between the two orbits. Although the uncertainties in Peißker et al. (2024b) are smaller by an order of magnitude, the key reason for this different orbit is their L′-band data point from 1999 which favors this newly derived orbit.

In order to test if the results of our work are affected by the X7 orbit choice we repeated the analysis but making use of the orbit derived by Peißker et al. (2024b). The calculations showed that the closest stars to X7 within the last 200 years are at least 4000 au apart (see right-hand side panel of Figure B.1). Bear in mind that our original separation threshold was 1000 au. As in this case the separation is at least four times larger the use of a different orbit makes less likely the relation to any of the star candidates.

Appendix C: Simulated morphology evolution

For completeness, we analyzed all the Br-γ observations available and compared them with the simulated emission. Figure C.1 shows the sky-projected Br-γ flux observed from Earth through the epochs t = 2006, 2008, 2009, 2010, 2011, 2012, 2013, 2014, 2017, 2018, 2019, and 2021. Each panel corresponds to 1″× 1″with Sgr A* located on the uppermost left-hand side corner. The simulated Br-γ flux is shown as colormap whereas the observed emission is depicted as colored contours. Notice that the observations contain most of the distribution of the simulated flux, and the emission level is of the same order as the reported values as it is shown in the main text.

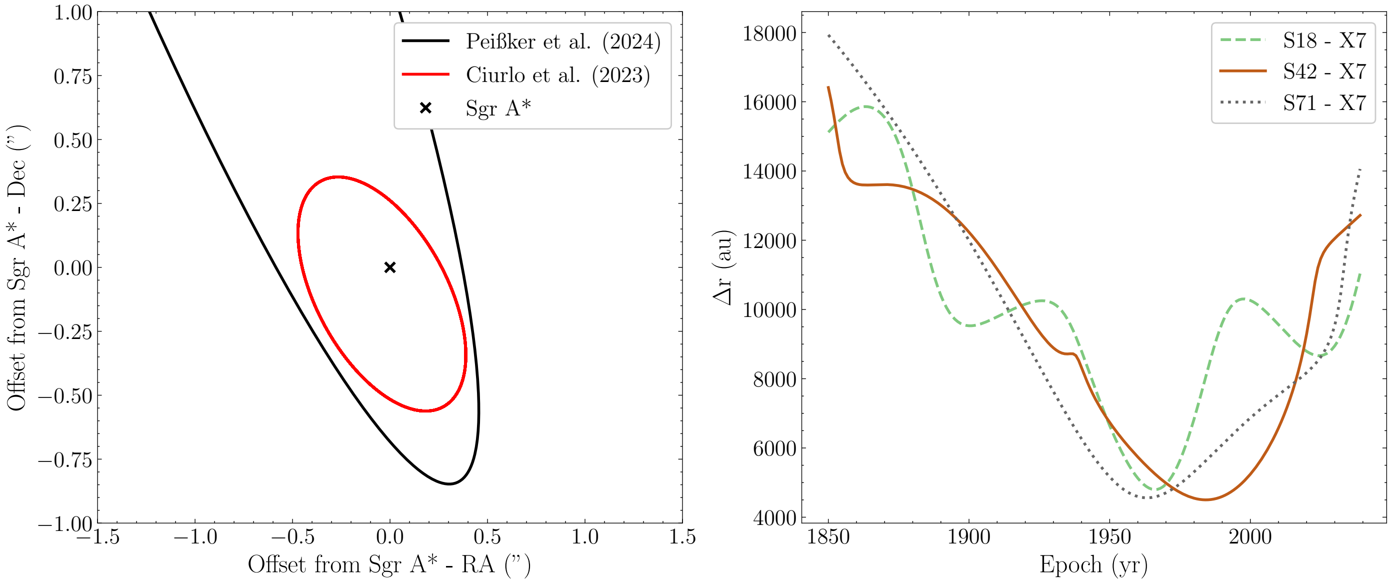

Fig. B.1: The left-hand side panel shows a comparison of the best fitted orbits of X7 projected on the sky by (Ciurlo et al. 2023) and (Peißker et al. 2024b) which are shown as solid black and red lines, respectively. The right-hand side panel shows the three-dimensional separation between X7 and candidate stars to constrain its origin based on an alternative orbital solution for X7 (Peißker et al. 2024b) as a function of time. The three stars shown, S18, S42, and S71 have fully constrained orbits (von Fellenberg et al. 2022). Notice that their closest approach to X7 over the past 200 years is between 1950 and 2000 at a three-dimensional separation >4000 au.

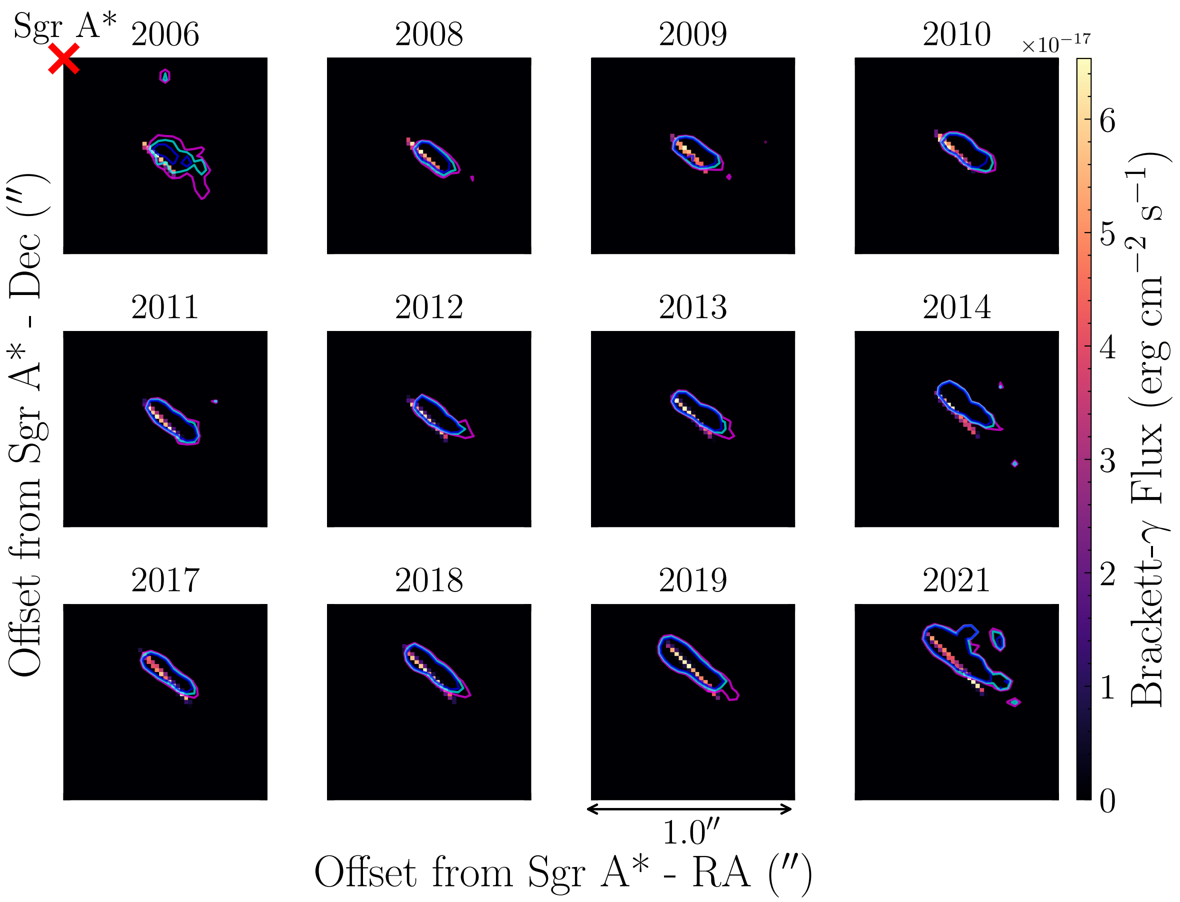

Fig. C.1: Comparison of the morphological evolution of X7 and the simulated cloud. The panels show sky-projected $1'' \times 1''$ Br-γ images highlighting the emission from X7 with contours in the period 2006-2021. The simulated cloud is overlaid with colored markers that encode the simulated Br-γ flux. The position of Sgr A* is on the top left corner of each panel. North and East directions are up and left, respectively.